Astronomy & Astrophysics manuscript no.
(DOI: will be inserted by hand later)
April 20, 2004

HST, VLT and JCMT observations of the disk and bipolar outflows of the planetary nebula NGC 6302 ⋆ ⋆⋆

M. Matsuura[1], A.A. Zijlstra[1], F.J. Molster[2], L.B.F.M. Waters[3,4], H. Nomura[1], R. Sahai[5], M.G. Hoare[6]

[1] Department of Physics, UMIST, P.O. Box 88, Manchester M60 1QD, UK
[2] ESTEC/ESA, Keplerlaan 1, 2201 AZ Noordwijk, The Netherlands
[3] Astronomical Institute 'Anton Pannekoek', University of Amsterdam, Kruislaan 403, 1098 SJ, Amsterdam, The Netherlands,
[4] Instituut voor Sterrenkunde, Katholieke Universiteit Leuven, Celestijnenlaan 200B, 3001 Heverlee, Belgium
[5] Jet Propulsion Laboratory, California Institute of Technology, MS 183-900, 4800 Oak Grove Drive, Pasadena, CA 91109, USA
[6] Department of Physics and Astronomy, University of Leeds, Leeds LS2 9JT, UK

Received 2004; accepted

Abstract. The famous 'butterfly' planetary nebula, NGC 6302, shows a unique combination of characteristics: a dense equatorial dust disk, bipolar flows, a mixture of crystalline silicates and PAHs, and an unobserved, very hot central star. We present Hubble Space Telescope (HST) Hα and [N II] images, Very Large Telescope (VLT) L- and M-band images at 0.4-arcsec resolution, including Brα and PAH images, and JCMT 450 μm image. VLA 6 cm continuum data (Gómez et al. 1989) are also re-analyzed. Extinction maps trace the structure of the equatorial disk. We find extinction $A_{\mathrm{H}\alpha}$=5–7 mag in the disk and the disk is optically thick even in the near-infrared ($A_{\mathrm{Br}\alpha}$=1–2 mag). The 450 μm map shows a north-south elongated central core, tracing the massive dust disk, and extended emission from dust in the bipolar flows. A fit to the SED shows a disk mass of 3 $M_\odot$. The HI (VLA) and H_2 (ISO) masses are much lower: we suggest that the lines from these species, especially H_2 originate from the heated surface of the disk. The innermost region shows a hollow, ionized shell surrounded by protuberances blown by the hot central star colliding with the disk. The orientation of the core, disk and lobes are markedly different. The outflow structures are well described by the warped-disk model. The PAH emission is found in the outflow and protuberances, in shock- and UV-heated gas. NGC6302 has a C/O ratio < 1: the PAHs form in oxygen-rich gas. We suggests PAH formation occurs in the heated surface of the disk, starting from CO photo- or shock-dissociation.

Key words. Planetary nebulae:individual:NGC 6302 – ISM:dust, extinction – Stars:imaging – Infrared: stars – submillimeter

1. Introduction

Low- and intermediate-mass stars (about 1–8 $M_\odot$) lose 20–80 per cent of their mass during the Asymptotic Giant Branch (AGB) phase. During this short phase (10^3–10^4 yr) mass-loss rates are as high as 10^{-7}–10^{-4} $M_\odot$ yr^{-1}. Subsequently, the stars evolve to the post-AGB phase, and the ejected mass forms a planetary nebula (PN). Many PNe and post-AGB nebulae show asymmetric shapes: elliptical, bipolar or multipolar (e.g. Sahai and Trauger 1998; Balick and Frank 2002). There is so far little evidence of asymmetric outflows in AGB stars (e.g. Zijlstra 2001a; Zijlstra et al. 2001b). The change of shape must be triggered at the beginning of post-AGB phase, and amplified by the fast wind of the PN central star (Kwok 1982). The most extreme morphologies appear to be related to circumstellar disks and their interaction with the hot stellar wind (Balick 1987). Disks, when observed around evolved stars, may indicate binarity (e.g. Van Winckel et al. 1999): they are commonly found around young post-AGB stars but rarely around PNe. Observations of disks are a key to understanding the current (bipolar) shapes, and their relation to the disk properties and formation history.

NGC 6302 is a well-studied planetary nebula, known for its spectacular bipolar optical morphology resembling a butterfly. A central dark lane extends from north to south, making NGC 6302 one of the few examples of an evolved, hot star still retaining a disk. The central star has never been detected but it is believed to be one of the hottest PN central stars known (Pottasch et al. 1996). The disk is perpendicular to the major axis of the 'butterfly'-shape outflow. However, the 6-cm radio continuum shows an ionized, toroidal structure located behind the obscuring disk, which is inclined at about 45 degrees to the

Send offprint requests to: M. Matsuura (m.matsuura@umist.ac.uk)

⋆ Based on observations made with the NASA/ESA Hubble Space Telescope, obtained from the ESA/ECF Data Archive. HST is operated by the Association of Universities for Research in Astronomy, Inc., under NASA contract NASA 5-26555. These observations are associated with program no. 8345.

⋆⋆ Based on observations with European Southern Observatory, Very Large Telescope with ISAAC (the proposal number 65.D-0395A).

optical major axis (Gómez et al. 1989). Therefore, the location and structure of the disk is under discussion, and a physical explanation for the multiple-axes structure is still lacking.

Both PAHs and crystalline silicates are detected in ISO spectra of NGC 6302 (Roche and Aitken 1986; Waters et al. 1996). This combination of carbon and oxygen-based chemistry is rare among post-AGB stars. Waters et al. (1998), and Molster et al. (1999) propose that in double-chemistry sources the crystalline silicates are found in the disk, while the PAHs are located in the outflow. NGC 6302 is the only object in this small group with a hot star: all other cases have cool stars, often late [WC] stars (Zijlstra 2001a). NGC 6302 is known to be oxygen-rich: the origin of the PAHs is problematic, as is discussed in this paper.

We have obtained deep optical and infrared image of NGC 6302, with subarcsecond resolution. VLT Brα and HST Hα images resolve the central region, and show evidence for a disk, flares and arcs. A 450 μm map shows dust emission both from the disk and from the outflow. In this paper we will use these new images to discuss the structure of the inner regions of NGC 6302.

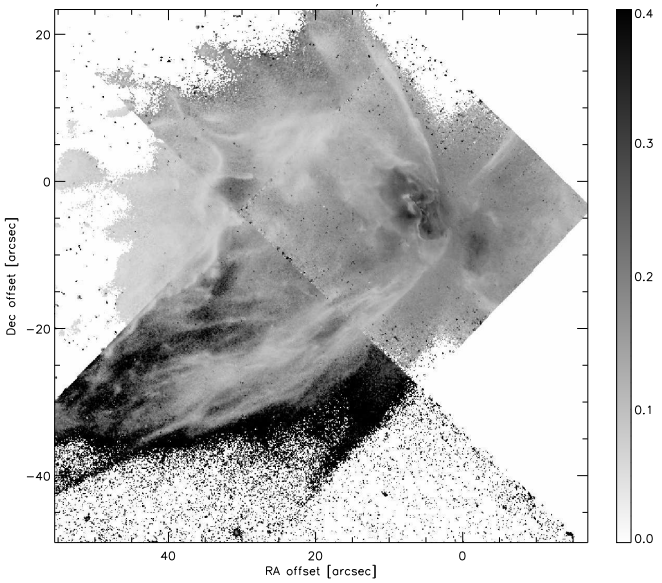

Fig. 3. The flux ratio of HST $F_{\nu\mathrm{F656N}}/F_{\nu\mathrm{F658N}}$ in Jy arcsec^{-2}. The ratio is assumed to be the Hα and N II intensity ratio, than Hα and continuum. The extinction does not work efficiently on this ratio because of a small wavelength difference in two bands.

2. Observations and data reduction

2.1. HST images

HST images were obtained using data archives at the Space Telescope - European Coordinating Facility (ST-ECF). The data were taken on the 22nd of February, 2000 with Wide Field Planetary Camera 2 (WFPC2), which has four 800×800 pixel detectors. The pixel scale is 0.046 arcsec for the Planetary Camera, which covers the most interesting region for this research, and 0.1 arcsec for the three Wide Field Cameras. Two filters were used, with exposure times of 610 sec (two 300 sec frames and one 10 sec frame) for the F656N filters and 470 sec (two 230 sec frames and one 10 sec frame) for F658N. The F656N filter (central wavelength 6564 Å, width 21.5 Å) mainly traces Hα emission, although some 6548 and 6584 Å [N II] emission is included in the passband (c.f. Dudziak and Walsh 1997). The F658N image (λ_0=6590 Å, $\Delta\lambda_0$=28.5 Å) suggests that 6584 Å [N II] emission may contribute up to 10 % of the inband flux of F656N image. Here, we use the F656N image as a Hα image. Pipeline-reduced data were used. The intensities are calibrated using the PHOTFLAM header parameter. Cosmic rays were removed by comparing four individual frames for the same region. The reduced images are shown in Figs.1 and 2. Fig. 3 shows the flux ratio of the two HST bands.

The HST images suffer from distortion. We use parameters in Anderson and King (2003) to obtain the corrected coordinate of each pixel. We use triangular linear interpolation to reconstruct the distortion-corrected image with a 0.071 arcsec grid, which is the same grid size as the infrared images. As a side effect of the interpolation the spatial resolution is reduced.

2.2. Near-infrared images

Near-infrared images of NGC 6302 were taken with ISAAC (Moorwood et al. 1999) at the ESO Very Large Telescope (VLT). The data was acquired on the 15$^{\mathrm{th}}$ of August 2000, in service mode. The weather was photometric. Filters used are summarized in Table 1. The obtained images are shown in Figs. 4 and 5. The 3.28 μm narrow (NB_3.28) covers the PAH bands with some contamination from Pfδ and He I 6–7, and the 4.07 μm narrow band (NB_4.07) contains the Brα line. There is no strong emission line known in the wavelength ranges of the narrow M-band (M_NB) and the 3.21 μm narrow band (NB_3.21) (e.g. Beintema and Pottasch 1999) and these bands show the continuum emission. The background was subtracted by chopping and nodding to a position 30 arcsec to the north-west, while keeping the source on the array. Some negative images of nearby stars apparent inside NGC 6302 are due to chopping (c.f. Fig.5). Jittering was used to improve flat-fielding. The total exposure times were 841 s in M_NB, 217 s in NB_3.21, 287 s in NB_3.28, and 411 s in NB_4.07, respectively. The pixel scale is 0.071 arcsec.

The optical seeing at the zenith varied between 0.4 and 0.85 arcsec. The full width half maximum (FWHM) in the frames were measured from a nearby star: it ranges between 0.3 and 0.4 arcsec. Some image-elongation is seen in the M-band. Results are summarized in Table 1.

We used *eclipse* and *IDL* for the data reduction. Detector non-linearity, significant at the brighter range, was corrected. The correction increases the flux per pixel of the calibration star by a maximum of 9 % in M_NB and 3–5 % in other narrow bands. The calibration star is HR 7446, a B0.5III star, with L′- and (wide) M-band magnitudes are 5.055 ± 0.010 and 4.996 ± 0.040 respectively (van der Bliek et al. 1996). Narrow-band magnitudes were derived by calculating colors for a 31,500 K black body to represent the B0III star (Tokunaga 1999). We assume that a 11 400 K black body (c.f. van der Bliek et al. 1996) has colors of zero at all the bands. Including the effects of filter and atmospheric transmission (Lord 1992),

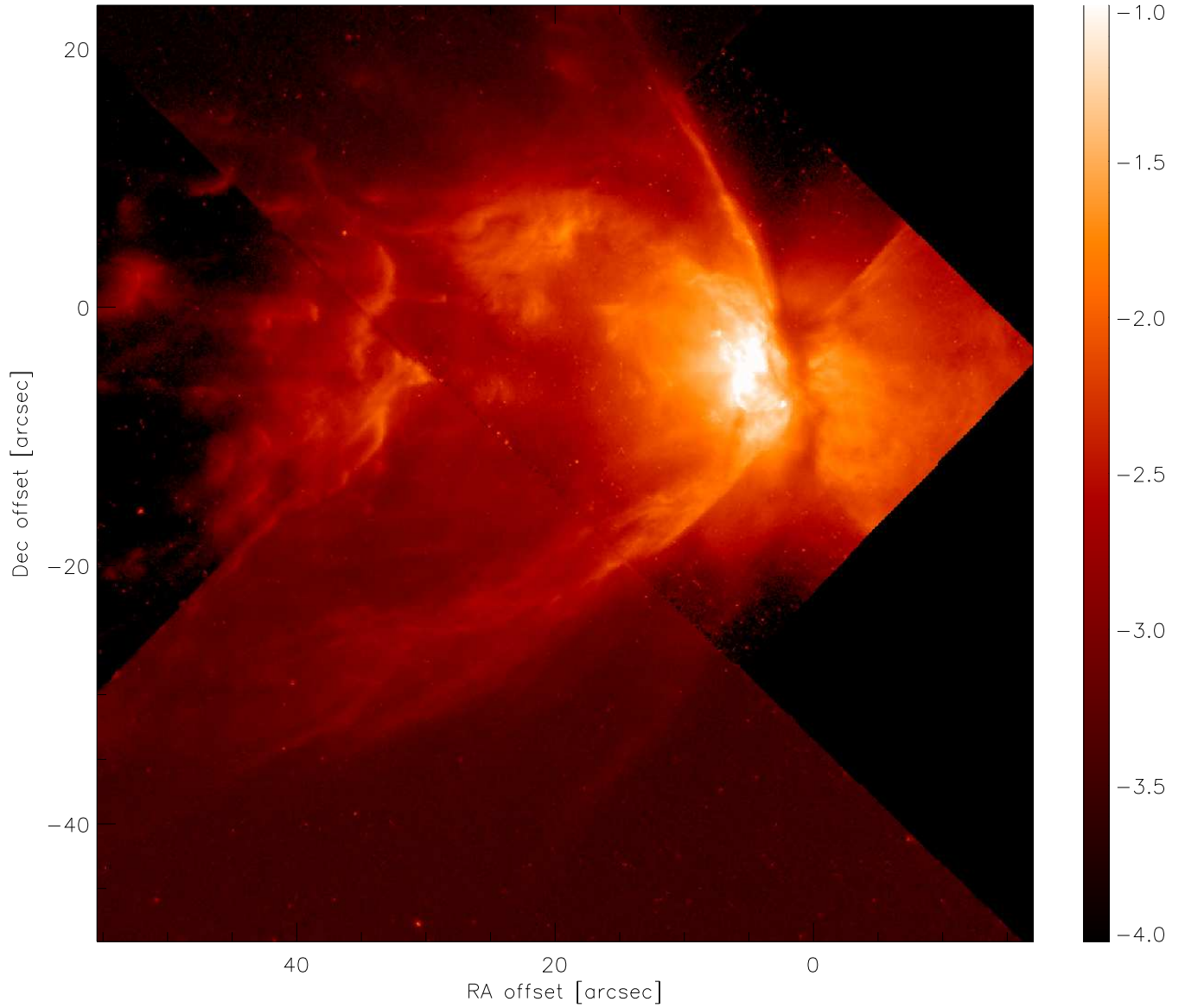

Fig. 1. The HST WFPC2 image in the F656N band (λ_0=6564 Å, $\Delta\lambda_0$=21.5 Å) before the distortion correction. The flux scale is $\log F_\nu$ in Jy arcsec^{-2}. This image is dominated by the Hα line, with some contribution from [N II] lines and continuum. The reference position is RA=17^{h}13^{m}44^s.2, Dec=−37°06′06″.1.

Online material:ngc6302_HST_wide_2color.ps

Fig. 2. The HST WFPC2 pseudo-color image combining the F656N (Nα) and the F658N ([N II]) filters. Blue represents F658N band. The [N II] lines are strongest in the outer regions.

Table 1. Filters, image quality and fluxes. The central wavelengths (λ_0) and the widths of the filters are listed. $F_{\nu 0}$ is calculated flux at the zero-magnitude, and F_ν is the flux of NGC 6302 through a 12.8 arcsec aperture. The optical seeing and the FWHM of the point spread function in the east-west (EW) and north-south (NS) directions are given.

Band	λ_0	$\Delta\lambda$	$F_{\nu 0}$	F_ν	Optical seeing	FWHM	
						EW	NS
	[μm]	[μm]	[Jy]	[Jy]	[arcsec]	[arcsec]	
M_NB	4.66	0.10	174.12	10.40	0.41–0.57	0.37	0.27
NB_3.21	3.21	0.05	343.40	1.95	0.51–0.74	0.37	0.43
NB_3.28	3.28	0.05	331.02	6.33	0.47–0.62	0.34	0.39
NB_4.07	4.07	0.07	223.85	10.29	0.44–0.84	0.28	0.31

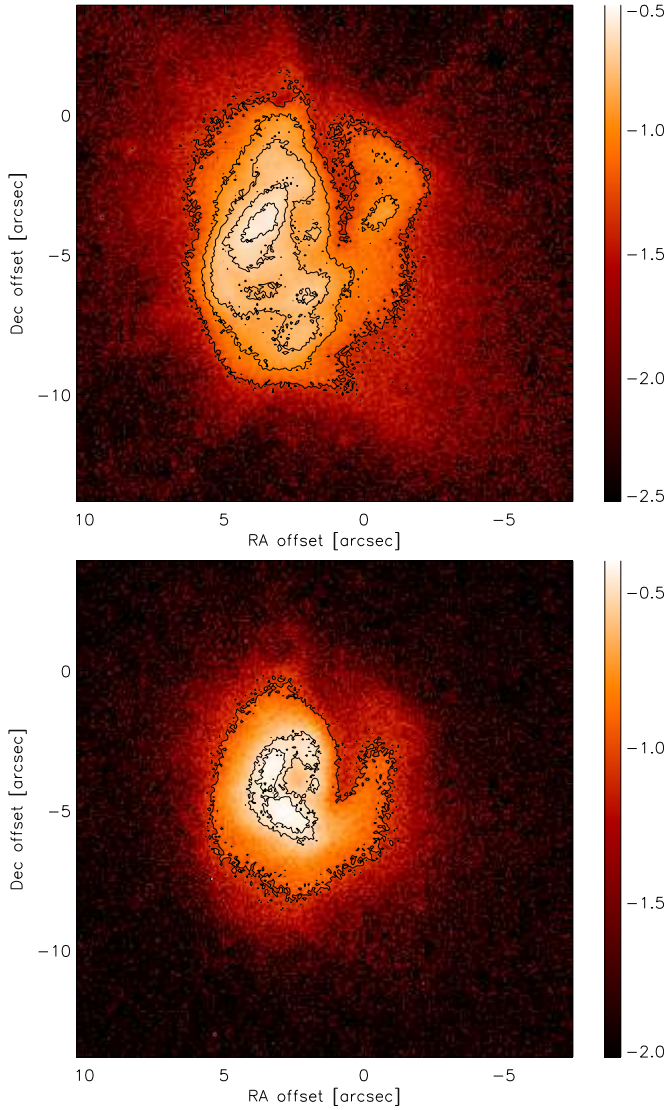

Fig. 4. The NB_4.07 image, which represents Br$_\alpha$ (top) and its nearest continuum, M_NB images (bottom). The flux scale is log F_ν in Jy arcsec^{-2}. Contour lines show 0.05, 0.1, 0.15, 0.2, 0.25 Jy arcsec^{-2} in NB_4.07 image, and 0.1, 0.3, 0.35 in M_NB image.

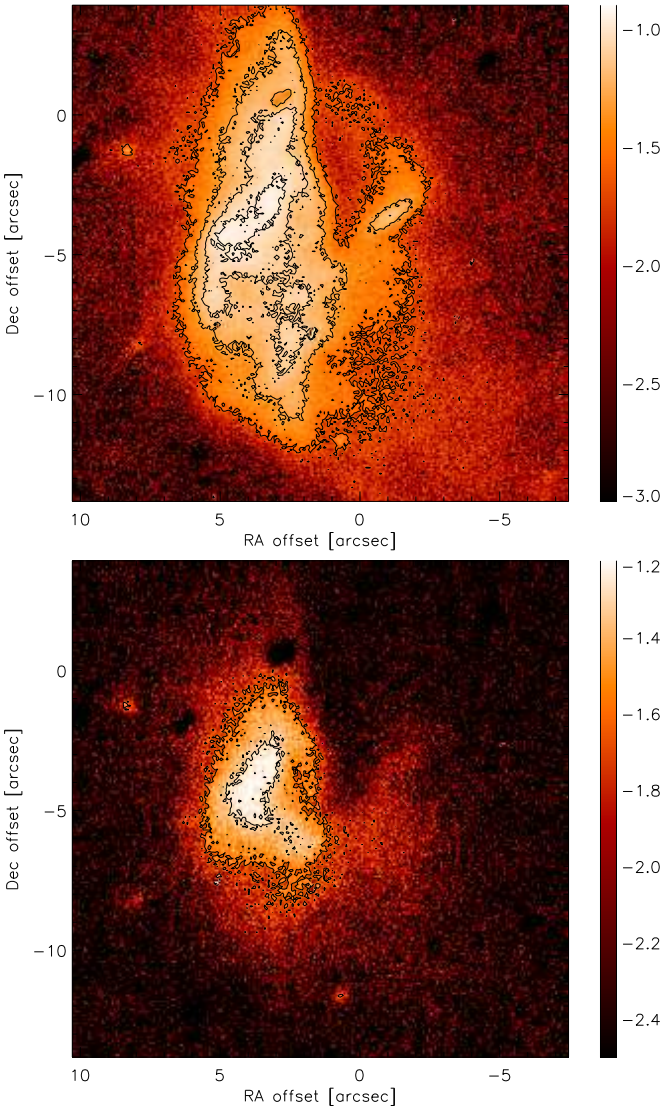

Fig. 5. The NB_3.28 image (top) and its continuum band NB_3.21(bottom). The flux scale is in log F_ν in Jy arcsec^{-2}. Dark spots at RA offset = 3, Dec offset = 1, and RA offset = 6 Dec offset = −2 are negative images of nearby stars, due to chopping. Contour lines show 0.025, 0.05, 0.075, 0.1 Jy arcsec^{-2} in NB_3.28 image and 0.025, 0.05 Jy arcsec^{-2} in NB_3.21 image.

we obtain NB_3.21 − L' = −0.025, NB_3.28 − L' = −0.017, L' − NB_4.07 = −0.010. We have assumed that the magnitude of HR 7446 at M_NB is the same as that for wide-band M. Although HR 7446 does not have strong hydrogen emission (Mennickent and Vogt 1988), the assumption of NB_4.07 may produce a systematic flux error.

Aperture photometry of NGC 6302 is listed in Table 1, together with fluxes for zero magnitude ($F_{\nu 0}$ in Jy). The aperture is centered on RA=17^{h}13^{m}44^s.3, Dec=−37°06′06″.4 (J =2000) and has a radius of 12.6 arcsec. The accuracies are estimated as about 10 % in L-band and possibly up to 20 % in M_NB.

The ISAAC RA coordinates of seven nearby stars are about 0.5–1.5 arcsec west of the 2MASS coordinates. Here we present the coordinates based on ISAAC. We use the VLT optical image (ESO 1998) as a reference, together with the 2MASS data, to find the alignment between the VLT infrared images and optical images. Two stars are in common in the infrared and optical VLT images, as well as 2MASS (2MASS names are 17134414−3706361 and 17134175−3706085). A systematic offset is also apparent between the HST and VLT images. We shift the HST image, referring to the optical VLT image (see 2.2). The central region of the corrected image is shown in Fig. 7.

Fig. 6 shows the alignment of infrared and optical images. The brightest infrared source is off-center, inside the optical eastern lobe; this is also the brightest position in the optical.

2.2.1. The Brα image

The Brα image (Fig. 7) is obtained from the NB_4.07 image (equivalent width of the filter is 0.62 μm), by subtracting a continuum image, which we interpolate from the NB_3.21 and

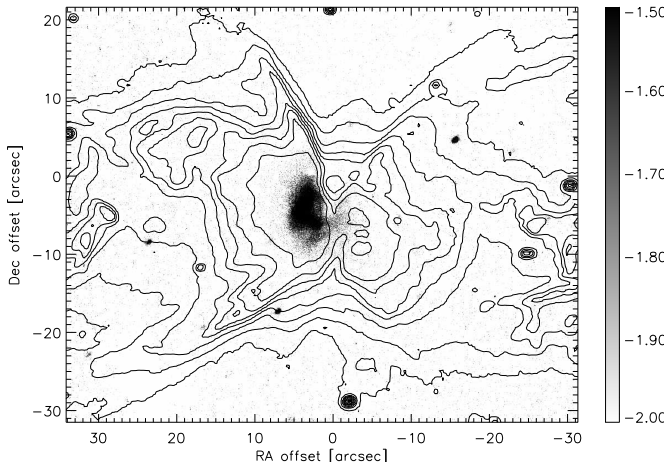

Fig. 6. ISAAC/VLT NB_3.21 color plot (log F_ν in Jy arcsec^{-2}) with contours of an VLT optical RGB composite image (ESO 1998). (The RGB composite does not show physical values; inside the east lobe the VLT optical image is saturated.) The brightest infrared source is located within the optical east lobe seen, and not at the optical dark lane.

M_NB images. At RA offset =2–3 and Dec offset = −4 – −6, the Brα flux becomes negative (−0.01 – −0.03 Jy arcsec^{-2}) after continuum subtraction. The large M_NB flux at this position indicates dust excess. Fig.9 shows the intensity profile along RA offset=−2.2: the flux peak in M_NB is found at −5.5 arcsec Dec offset, while other bands peak at −6.5. The values of Brα in this negative region is about 10 % of M_NB and this is comparable to the error in M_NB which has the largest uncertainty of all ISAAC images. The continuum flux in other regions is about 30–45% of the NB_4.07 flux.

Hydrogen bound-free emission has jumps at 3.28 μm and 4.47 μm, which corresponds to the series limit at n=6–∞ and n=7–∞. If the electron temperature is of the order of 10^4 K, the continuum estimated from NB_3.21 and M_NB has less than 1 % uncertainty with respect to the total bound-free and free-free emission, however this becomes about 10 % if the electron temperature is 10^3 K, as may be the case locally (Liu et al. 1995).

The total Brα intensity, measured through increasing circular apertures of 3.2, 7.1, 10.6 arcsec radius, on the center of the nebulae (RA offset = 1.846 and Dec offset = −4.260 arcsec), gives 1.6×10^{-11}, 4.8×10^{-11}, 5.0×10^{-11} erg cm^{-2} s^{-1}, respectively. Beintema and Pottasch (1999) measured a Brα intensity of 1.538×10^{-11} erg cm^{-2} s^{-1}, using the 14"×20" ISO/SWS aperture. They report that 50% or more of the flux is missing since the ISO/SWS aperture is not large enough to cover the whole nebula. However, the large discrepancy with our values suggests that either the ISO aperture was not well centered on the nebula, or that Brα flux is too high. If that is the case, the extinction at the wavelength of Brα may be underestimated.

2.3. The extinction map

We derive the extinction map of NGC 6302 from the ratio of the Brα or Hα with the 6-cm continuum data of Gómez et al. (1989). We use the HST image (Fig. 7) directly as the Hα flux,

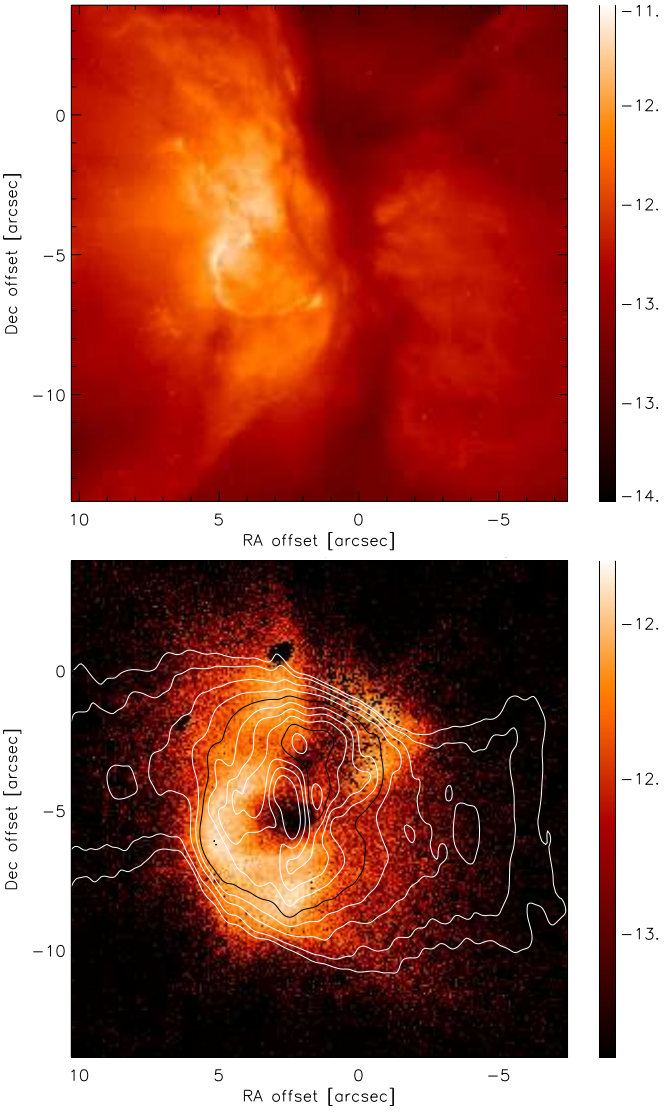

Fig. 7. (Top) The central region of the Hα image taken by HST. The flux scale is log I_ν in erg cm^{-2}s^{-1}arcsec^{-2} unit. (Bottom: color) The Brα (NB_4.07) image after continuum subtraction. The flux scale is log I_ν in erg cm^{-2}s^{-1}arcsec^{-2} unit. (Bottom: contour) The radio 6 cm continuum contours. The peak is 0.0479 Jy arcsec^{-2}. Contour lines are 0.0025, 0.005–0.045 Jy arcsec^{-2} with 0.005 Jy arcsec^{-2} grid, and 0.02 and 0.04 Jy arcsec^{-2} lines are shown in black.

as the continuum contribution is minor. Gómez et al. (1989) present a 6-cm continuum map, obtained with the VLA (observations taken 14 July 1987). We retrieved the data from the VLA archive. The data was reduced using the AIPS package, using uniform weighting in the UV plane. The beam size is 1.05 × 0.25 arcsec, with a position angle of 5 degrees. The cleaned image is shown overlaid on the Brα image in the bottom panel of Fig. 7. We aligned the 6-cm image with the Hα and Brα images so that the arc (c.f. Fig.12), and flares (RA offset∼ 4, Dec offset∼ −3, RA offset∼ 2.5, Dec offset∼ −2, and RA offset∼ −2, Dec offset∼ −3) coincide. The brightest spots in Hα, Brα, and 6 cm coincide inside the east lobe. The Hα and Brα images are smoothed to the spatial resolution of the 6cm image.

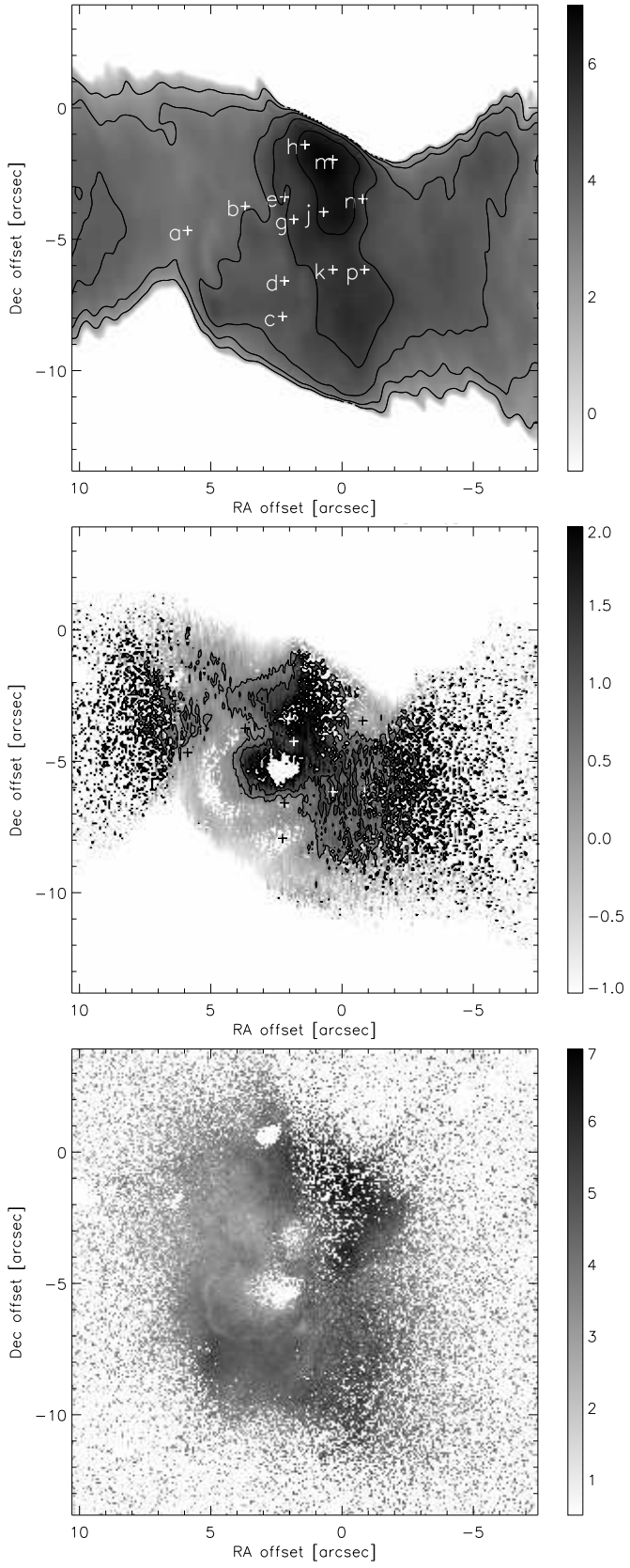

Fig. 8. Extinction maps derived from and Hα and 6 cm (top), Brα and 6 cm (middle), and the color excess E(Hα − Brα)(bottom) in magnitudes. Crosses show the positions for which extinction is summarized in Table 2. Contour levels: 2, 3, 4, 5, 6 mag (Hα image), 0.5, 1.5 mag (Brα image).

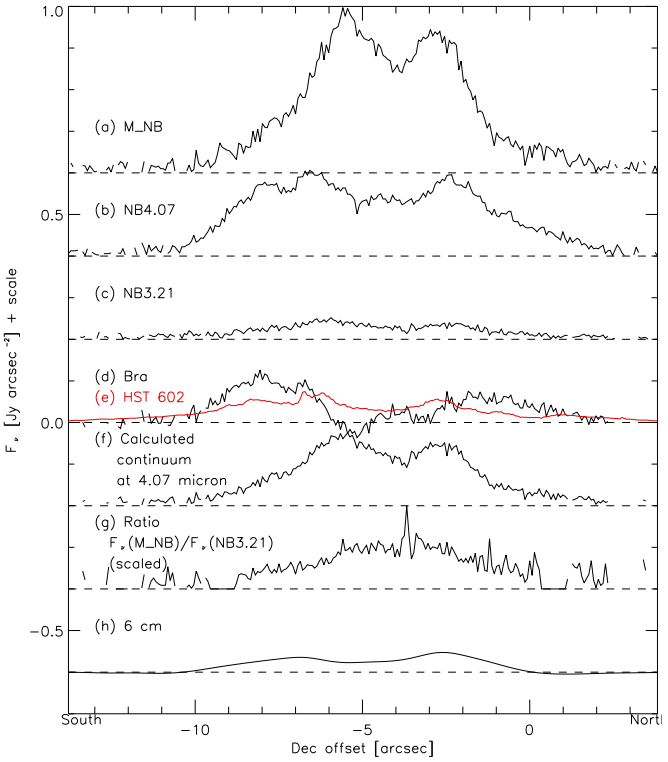

Fig. 9. Image slices at RA offset = 2.2. There are two peaks near the center in all bands, and M_NB has the smallest distance between the two peaks. The negative values of Brα is related to the M_NB peak, however the value is comparable to the error of M_NB which is used to estimate the continuum at Brα wavelength.

The extinction is estimated following Milne and Aller (1975) under the assumption of case B. The effective coefficient for Hβ is taken from Kwok (2000), and the effective ratio of Brα or Hα to Hβ, for an electron temperature (T_e) of 10^4 K and electron density of 10^4 cm^{-3}, are taken from Hummer and Storey (1987). We adopt $T_e = 1.8\times10^4$ K as given in Milne and Aller (1975). The effective coefficient is insensitive to electron temperature around 10^4 K (Hummer and Storey 1995). The extinction maps are shown in Fig. 8, and values of $A_{Br\alpha}$ and $A_{H\alpha}$, at representative places (most of them are local maxima or minima) are summarized in Table 2.

The interstellar extinction is estimated from two nearby stars (HD 155464 and HD 155364). The result is $E(B-V)$=0.34 mag kpc^{-1}, and $A(V)$=1.1 mag is of interstellar origin. We adopt a distance of 1 kpc ; previous distance estimates range from 0.15–2.4 kpc Meaburn and Walsh (1980); Rodríguez and Moran (1982); Kemper et al. (2002) find 0.91 kpc.

2.4. The JCMT sub-millimeter image

NGC 6302 was observed with SCUBA/JCMT (Holland et al. 1999) on 15 April 1998. Two bands (narrow band 450 and 850 μm bands) were observed simultaneously. The background was subtracted with chopping by 120 arcsec in longitude. The object was observed in 'jiggle map mode', and several images with slightly different positions were co-added. The atmospheric opacity (τs) was estimated from the measured τ

Table 2. The extinction including the interstellar extinction. Brα and Hα intensities ($I_{\mathrm{Br}\alpha}$ and $I_{\mathrm{H}\alpha}$) are in log erg cm^{-2}s^{-1}arcsec^{-2} unit. 6 cm intensity ($I_{\nu=6\mathrm{cm}}$) is in Jy arcsec^{-2}.

	position		$I_{\mathrm{Br}\alpha}$	$I_{\mathrm{H}\alpha}$	$I_{\nu=6\mathrm{cm}}$	$A_{\mathrm{Br}\alpha}$	$A_{\mathrm{H}\alpha}$	$E(\mathrm{H}\alpha-\mathrm{Br}\alpha)$
	[arcsec]	[arcsec]			$\times10^{-2}$	[mag]	[mag]	[mag]
a	5.89	−4.69	−12.39	−12.27	1.20	0.03	3.46	3.61
b	3.69	−3.76	−12.04	−11.88	3.64	0.40	3.85	3.52
c	2.27	−7.95	−11.85	−12.22	2.84		4.43	
d	2.20	−6.60	−12.05	−12.12	3.43	0.24	4.45	4.08
e	2.20	−3.41	−12.61	−12.34	3.65	2.78	4.99	3.20
g	1.85	−4.26	−12.33	−12.39	3.89	1.34	5.25	4.04
h	1.42	−1.42	−12.70	−13.07	2.67	1.74	6.36	4.83
j	0.71	−3.98	−12.69	−12.86	3.47	2.17	6.17	4.34
k	0.35	−6.18	−12.52	−12.61	2.19	1.19	5.26	4.11
m	0.35	−1.99	−12.49	−13.23	2.81	1.24	6.83	5.75
n	−0.78	−3.48	−12.02	−12.56	2.14	−0.19	5.15	5.25
p	−0.85	−6.18	−12.75	−12.87	1.52	0.72	5.30	4.19

at 225 GHz: we find about $\tau = 0.12$ at 850 μm, and 0.50–0.52 at 450 μm. The beam widths are approximately 7 arcsec at 450 μm and 13 arcsec at 850 μm. The data were reduced with the *Starlink software ORAC-DR* and *surf*. We can not accurately align the JCMT data to other data. The position of Fig. 10 is based on the FITS header, and not corrected to fit with ISAAC data.

The flux conversion factors (volts to Jy per beam) were obtained by the observatory only for point sources (855 and 248 Jy per beam per volt at 450 μm and 850 μm, respectively). These conversion factors applied to the peak fluxes, yield 38.9 Jy at 450 μm and 5.8 Jy at 850 μm. Due to the uncertainty of atmospheric opacity, and flux conversion factors, the flux accuracy may be as much as 50 % in error. The point-spread function is unknown, with significant flux in the side lobes of the beam. The total extended 450-μm flux is an underestimate by an unknown amount. Hoare et al. (1992) reported 46 Jy at 350 μm, and 3.82 Jy at 800 μm.

According to spectra in Hoare et al. (1992), about 90 % of the flux at 450 μm is dust emission, while the remaining 10 % is free-free emission from the ionized gas. This is less clear for the wings. The wings have a 6 cm flux less than 0.0025 Jy arcsec^{-2}, which predicts less than 0.5 Jy per beam at 450 μm. The 450 μm flux is less than 1 Jy per beam in the lobes. However, assuming that the beam is approximately Gaussian, about 55 % of the flux comes from the lobes. Compared with the 10 % contribution from free–free emission, which mostly comes from the core region, leads us to a conclude that the 450 μm map largely traces the dust emission here as well.

The 850-μm resolution is lower, and below we will only use the 450-μm image.

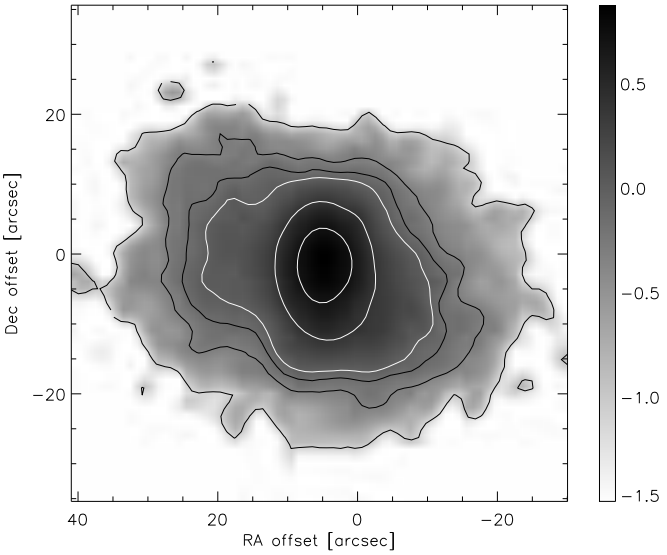

Fig. 10. SCUBA/JCMT 450 μm image in log F_ν in Jy per beam. The contour lines show 0.1, 0.5, 0.75, 1.0, 2.5, 5.0 Jy per beam. The position is according to the observatory information, and not registered to the ISAAC data.

3. The Results

3.1. The central region

The HST image (Fig. 11) shows a dark lane running from north to south (Fig. 12). It extends from (RA offset, Dec offset) = (0, 0) to (0, −8), and we find a clear edge on the north side. Limb-brightening of the disk is found in (RA offset, Dec offset) = (0, −3) arcsec. The high excess extinction and relative thinness suggest that this dark lane is a dusty disk. Flares and arcs near the disk resemble collimated outflows, such as found in the proto-planetary nebula, Frosty Leo (Sahai et al. 2000).

Fig. 6 shows that the brightest infrared emission is located within the east lobe, which confirms the claims by Latter et al. (1995) and Kemper et al. (2002). Lester and Dinerstein (1984) claimed that the bright infrared source in K- and N-bands is coincident with the optical dark lane, however our alignment does not agree with this. The optical dark lane is still dark at infrared wavelengths, as seen in Figs. 5 and 7. There are two discrete components in the spectral energy distribution (SED) (Kemper et al. 2002). Hot dust is detected in near-infrared images, and its color temperature is about 360–470 K (NB_3.21 − M_NB 3–2 mag; Fig. 13). Cold dust is likely located in the disk. The JCMT image detects this dusty, cold disk.

The disk as measured in the Hα image (Fig. 7) extends at least 8 arcsec to the north. The boundary in the southern di-

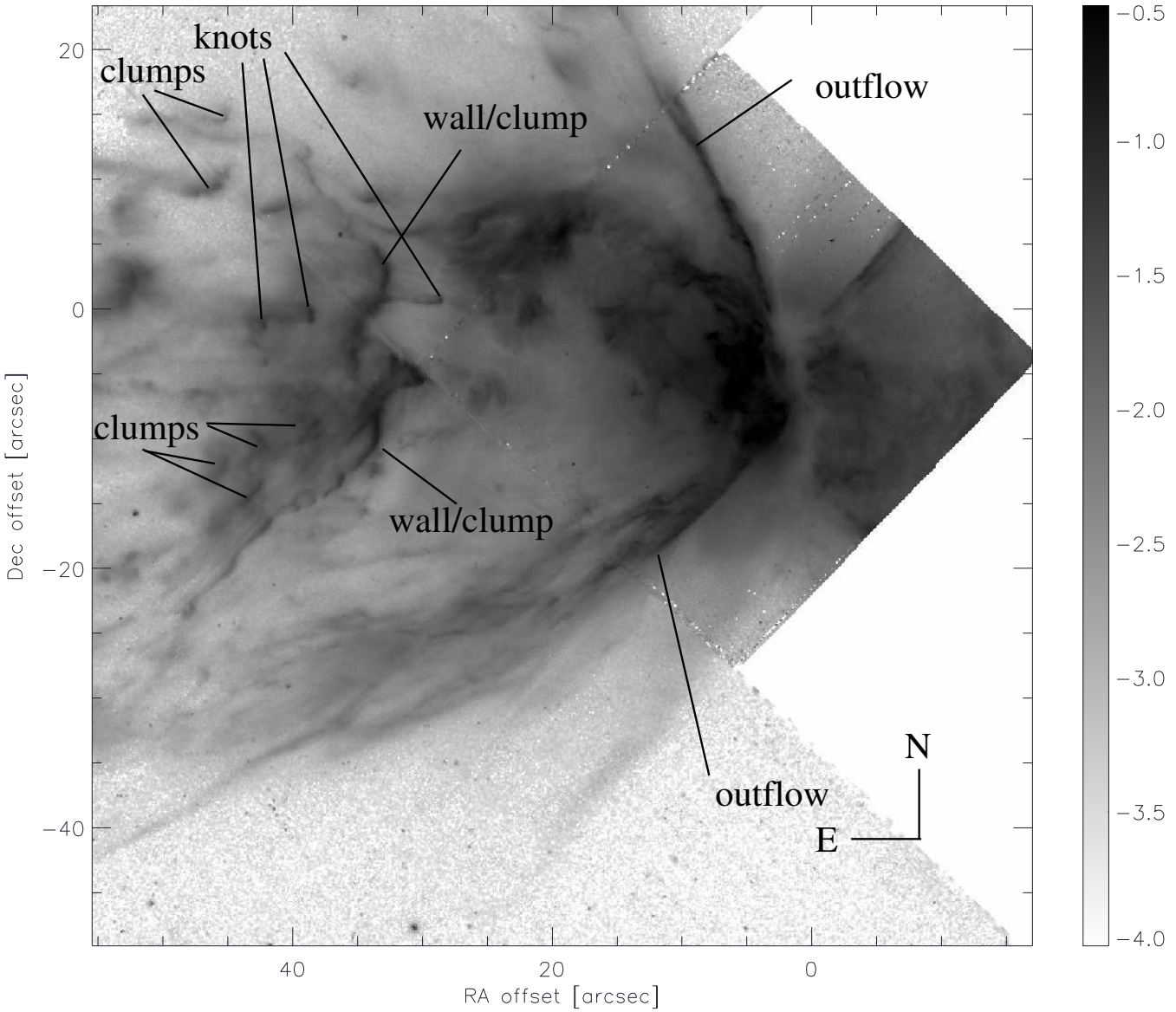

Fig. 11. Schematic view of outer region of NGC 6302 overlaid on the HST F658N image, which shows more complicated structure than Hα image. The flux is calibrated as $\log F_\nu$ in Jy arcsec^{-2}.

rection is not clear. This outer radius represents the highest optically depth in the disk towards our line of sight, and the actual size of the disk could be larger than this measured size. The JCMT 450 μm image shows a FWHM of 15.0 arcsec in the north-to-south direction, and at the 3 σ level extends 31 arcsec (where σ is the error estimated from the area between 80 and 100 arcsec away from the peak). The thickness of the disk is not uniform: it is about 1 arcsec in the inner region, widening to about 4 arcsec at the outer edge in Hα image.

From the semi-ellipse appearance of the disk in Hα image, we estimate its inclination to the line of sight as $\sim$ 20 degrees. The disk absorption is seen on the western side. The (more distant) optical lobes are also fainter on the western side, partly due to the additional extinction but we also find evidence that the eastern, brighter lobe is intrinsically more massive. The brightest region at near-infrared wavelengths could correspond to an inner part of the disk.

Several arc-like feature around the dark lane (Fig. 12). The Brα emission (Fig. 7) also traces the arcs. One of the explanations for a bipolar 'butterfly' shape is the interaction of the fast wind with a disk formed on the AGB (Balick 1987). The flares and arcs indicates such an interaction. The outer edge of the interaction front is clearly seen in the Hα image.

The central region has high Hα/N II ratio (Fig. 3) than the surrounding region. This shows either high temperature or high density of ionized gas. Bohigas (1994) suggested latter case.

The Brα shows a lack of emission at the location of the central hole in the 6 cm map (RA offset, Dec offset) = (2.5, −5) arcsec : this likely corresponds to the inner cavity of the shell (Fig. 9). The cavity is not evident from the HST image, because of significant circumstellar extinction. The exact centroid of the cavity is not unambiguously identified. In the radio, the brighter emission to the North combined with the elongated beam partly obliterates it, while in Brα the dark lane hides the

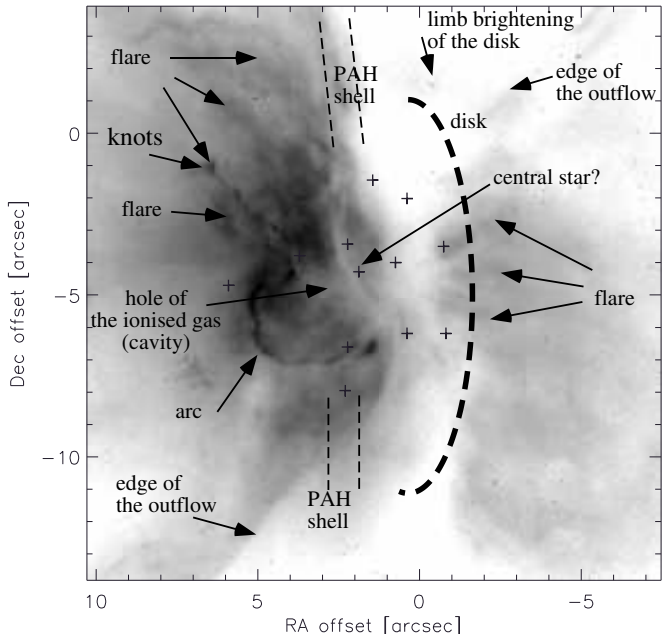

Fig. 12. Schematic view of central part of NGC 6302 overlaid on the HST Hα image. The structures seen in this image are shown with solid lines, and those seen in other bands are shown in dashed lines.

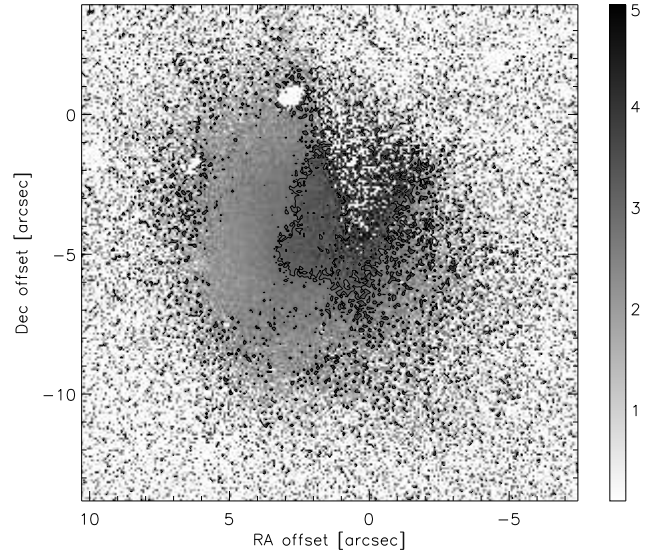

Fig. 13. The NB_3.21 and M_NB two-color image in magnitudes. Contour line is for 3.0 mag.

edge of the north-west extension. We assume an intrinsic cylindrical structure (giving a rectangular cavity in projection) such as seen in NGC 7027. The Brα extinction map (Fig. 8) shows the edges of the cylinder.

3.2. The outer region

The HST image (Fig. 11) shows a weakly collimated polar outflow. The outer low excitation region of the NGC 6302 shows several clumps and knots. All three knots show the wind tail to the east, pointing away from the star. Such knots are also found in the elliptical PN, NGC 2392 (O'Dell et al. 2002). The origin of knots could be either primordial or instability-related (e.g. Lopez-Martin et al. 2001). The clumps also have wind tails in approximately the eastern direction. The largest clumps are rather 'wall' like, indicative of gas compressed by the fast wind.

The knots in the outer lobes are in contrast to the knot in the central region (Fig. 12), which is located at the tail of a flare pointing *towards* the star. This knot appears to be accelerated by the fast wind. This type of knot is found in the proto-PN Frosty Leo (Sahai et al. 2000, the knot is on the far side of the central star of jets (J1 and J3)). In both the PN and proto-PN, these knots are found near the central star and around the 'disk' region. The formation should be related with collision of the fast wind with the disk.

3.3. Dust distribution

3.3.1. The extinction map

Casassus et al. (2000) estimate $A_V = 3.7$ averaged over a 3×3 arcsec^2 aperture. Pottasch et al. (1996) report $E(B-V)$=0.855 based on various methods, weighted towards the brightest region and this is equivalent with $A_V = 2.8$ if $R(V) = A(V)/[A(B) - A(V)] = 3.1$ mag (Mathis 1999). Bohigas (1994) reported $C(\mathrm{H}\beta)$=1.56 at the brightest location (equivalent with $A_V = 3.35$ mag). Our results show $A_{\mathrm{H}\alpha}$ of 3.46 (equivalent with $A_V = 4.24$ mag) and 3.77 (equivalent with $A_V = 4.61$ mag) at the bright regions (a) and (b). The slightly higher values are probably due to the higher spatial resolution. The highest values at the dark lane exceed $A_{\mathrm{Br}\alpha} > 1.0$ and $A_{\mathrm{H}\alpha} > 6.0$, at regions (h), and (m) (Fig. 8 and Table 2).

The interstellar extinction law predicts the relations $A_{\mathrm{Br}\alpha}/A_V = 0.042$, and $A_{\mathrm{H}\alpha}/A_V = 0.817$ for $R_V = 3.1$ (Cardelli, Clayton and Mathis 1989). At the dark lane, the expected $A_{\mathrm{Br}\alpha}$ is 0.3–0.4 mag. However, the measured $A_{\mathrm{Br}\alpha}$ is larger than 1.0 mag; the difference exceeds the error in the Brα intensity. This implies a grey extinction law in these regions, which would indicate large grain sizes. However, we have to be careful about possible oversubtraction of the continuum in Brα, which would give a too large extinction in Brα.

In the optical image, the western lobe is fainter than the eastern lobe, by about 1 magnitude, possibly because of larger extinction (e.g. Rodríguez et al. 1985). Our $A_{\mathrm{H}\alpha}$ shows that the extinction is only slightly larger in the western lobe. Both near-infrared continuum bands show that the eastern lobe is brighter, as does the radio 6-cm, which are less affected by dust extinction. This shows that the density is higher in the eastern lobe. Therefore, we conclude that more ionized gas is located in the east lobe than in the west lobe. This is consistent with Bohigas (1994) and Hα and N II ratio in our work.

3.3.2. PAH

PAH emission was found in NGC 6302 by Roche and Aitken (1986), Roche et al. (1996) and Casassus et al. (2000). (The 3.3 μm image in Casassus et al. (2000) is upside-down; Casassus private communication). Fig. 14 shows the PAH map, which is the continuum (NB_3.21) subtracted image of

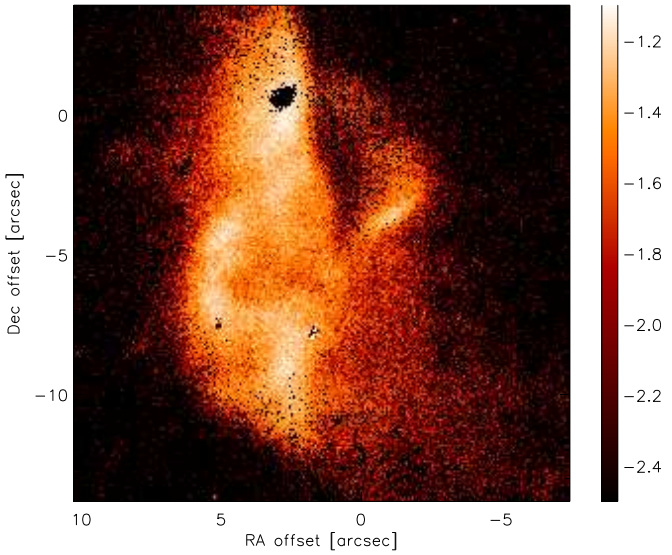

Fig. 14. The PAH image of the core region. The color is log F_ν in Jy arcsec^{-2}.

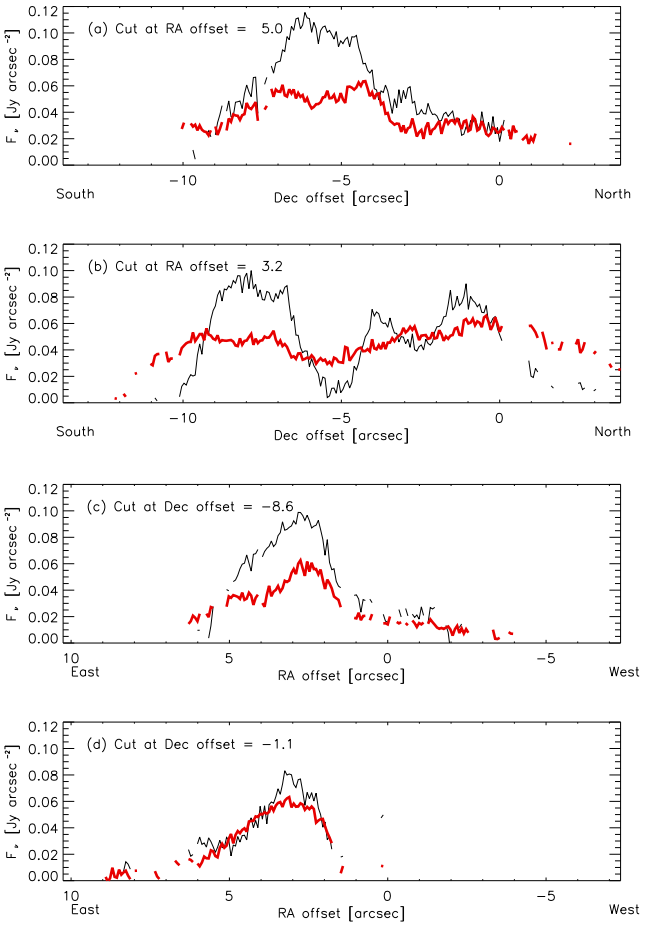

Fig. 15. PAH distributions (gray thick lines) along the north to south directions at RA offset = 5.0 arcsec (a) and at RA offset = 3.2 arcsec (b). For comparison, the Brα distributions are shown in black thin lines. Fluxes are averaged over the neighboring 5 pixels with the same Dec coordinates. (c) and (d) are the ones along east to west directions.

NB_3.28. The L-band spectra (Casassus et al. 2000) show some contamination by the Pfδ + He I 6–7 line in NB_3.28. This helium line contributes about 20–30% of the continuum subtracted intensity in NB_3.28 in the central 3×3 arcsec^{-2} region (Casassus et al. 2000). From TIMMI-2 observing, we argue that this 3.3 μm shows mainly PAH Kemper et al. (2002).

No clear PAH emission is found in the dark lane. Some emission in the southern part of the dark lane is interpreted as located in the foreground of the disk. The PAH distribution is similar to that found in the Red Rectangle (Waters et al. 1998) and IRAS 16279−4757 (Matsuura et al. 2004), which also have both PAH and crystalline silicates in a single (evolved) object, with the PAHs located in the outflow.

Fig. 15 shows the intensity distribution sliced along several directions at several locations. In the east-west directions (Fig. 15 (c) and (d)), the intensity peaks are identical in PAH and Brα. A slight difference is found only in the north-south direction at RA offset = 3.2 arcsec, near the dark lane (Fig. 15 (b)). At this position, PAH is more extended than Brα.

The PAH distribution in the planetary nebula NGC 7027 is more extended than the ionized gas (Woodward et al. 1989). PAH emission is more extended than the ionized gas in the Orion bar, but inner region of the H_2 gas (Sellgren, Tokunaga and Nakada 1990). Omont (1986) concluded that strong UV radiation from the central star destroys PAHs on the inner side of the nebulae. A similar multi-layer structure is implied inside the lobe of NGC 6302. The inner, ionized region of the lobe and the neutral outside are seen edge-on by us, and we can not see the difference in the intensity peaks in PAH and Brα in the east-west direction. However, in the north-south direction, we can see the difference in the radii of the PAH layer and the ionized gas layer.

Shock formation of PAHs is proposed by Omont (1986). The edge of the dark lane is the ideal place for a shock, where the outflow from the central star collides with the stable disk. Indeed, the PAH intensity has a local peak near the dark lane (RA offset = 3.2 arcsec).

Fig. 16 shows the entire NB_3.28 VLT image. This band shows a very faint shell located 25 arcsec to the northeast. No other infrared band shows emission this far out. We prefer this distant emission is due to PAH rather than to the He I line.

Persi et al. (1999) found that the 6.2 μm PAH distribution has two peaks (north and south peaks), while the 11.3 μm PAH image has a single peak corresponding to the southern peak of 6.2 μm image. The two 6.2 μm peaks are also found in our 3.28 μm PAH image. The 3.3 μm band is due to C-H stretch vibration, the 6.2 μm band is due to C-C stretch vibration, and the 11.3 μm band is due to C-H bending out of the plane (Allamandola, Tielens and Barker 1989). Persi et al. suggested that the north peak shows a different composition or dehydrogenation. Our results show that dehydrogenation is not the cause, because the 3.3 μm C-H stretch band is detected even at the north peak. A different composition (or smaller size) could suppress the northern peak at 11.3 μm.

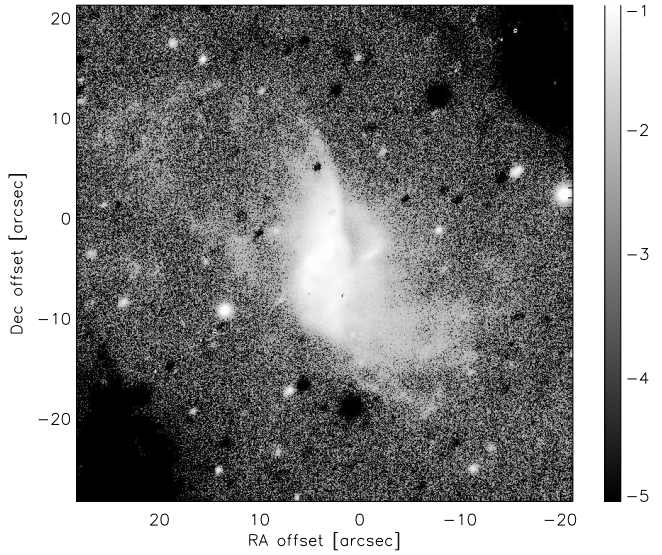

Fig. 16. ISAAC/VLT image of NGC 6302 in NB_3.28. The faint shell in the north-east is seen only at NB_3.28, and not in other infrared bands. The negative images of chopping are located at the corners of north-west and south-east. The color is $\log F_\nu$ in Jy arcsec^{-2}. Note that some of the stars in the images (both positive and negative) are artificial images created by shift-and-add of the chop-and-nodded images.

3.4. Modeling the JCMT 450 μm image

The JCMT 450 μm image shows that with about 45 % of the energy coming from the central 25 arcsec (Hoare et al. 1992, Fig. 10 in this work). The bright core at 450 μm is assumed to correspond to the dark lane (the dusty disk).

We fit the SED with a model distribution, using the radiative transfer code of Nomura (2002) and Nomura and Millar (2004). The dust grains are heated by the central star, and radiative transfer is solved in a spherically symmetric structure. The flux profile is calculated along the line accross the center with a thickness equal to the beam size. As long as the disk is edge-on, i.e., the central star is not directly seen, the assumption of the spherically symmetric structure will not cause a significant discrepancy in the calculated SED. Two different radial distributions of dust grains are used: $\rho = \rho_0(r/r_0)^{-1}$ and $\rho = \rho_0(r/r_0)^{-2}$, where ρ is the dust density, and r is the radius, and subscript zero shows the values at the inner radius. The dust-to-gas ratio is assumed to be 0.01, and the absorption coefficient of interstellar dust (Adams and Shu 1985, 1986) is used. The assumed parameters of the object are: distance of 1 kpc, luminosity of 2436 $L_\odot$ (obtained from IRAS data), and temperature of the central star 1×10^5 K.

The SED is fitted well with the model parameters $r_{\rm in} = 1 \times 10^{16}$ cm, $r_{\rm out} = 1 \times 10^{17}$ cm, and a gas mass of 3 $M_\odot$. The resulting fit is shown in Fig. 17 (a). The observed fluxes are obtained from this work (the flux from the central region is used for JCMT data), Hoare et al. (1992), and Milne and Aller (1982). The free-free emission of hydrogen is scaled to the 6 cm flux. The figure shows that we can ignore the contribution of ionized hydrogen to the infrared and submillemeter flux, except at 800 μm. Little difference is found in the calculated SEDs from the two density profiles.

Below 12 μm, the model flux is far below the observed values. This confirms that the SED of NGC 6302 can not be fitted with a single component (Kemper et al. 2002). The fit could be improved if the disk is inclined so that the hot inner region is seen directly. However, we can not distinguish between disk inclination and hot dust in the outflow; the near infrared flux is sensitive to both the inner radius of the disk, and to the inclination of the disk (a similar discussion is found in Lopez et al. (1997)).

The SED of NGC 6302 is similar to those of DUPLEX proto-PNe (Ueta et al. 2000), which have longitudinally extended nebula with a large dust emission, although NGC 6302 has a SED peak around 60 μm which is at longer wavelength than any proto-PN in the sample in Ueta et al.

The temperature profile (c) gives a dust temperature at the inner radius is about 100 K. If the inner radius is smaller, and the inner most dust temperature is closer to the sublimation temperature (about 1000 K), then the SED is not fitted: the SED peak is shifted towards 10 μm.

The calculated intensity profile is found in Fig. 17 (b). The profiles are smoothed with the beam, and compared with the observed profile (Fig. 17 d). Here we use the beam profile with three component Gaussian estimated by Hogerheijde, and Sandell (2000). Williams (2003) shows similar measurements two year after from Hogerheijde, and Sandell's measurements. The calculated north-south profile reasonably traces the observed one. The radial intensity profile is fitted better with the r^{-1} density distribution.

The analysis implies an envelope of 3 $M_\odot$ (dust-to-gas ratio of 0.01); a density distribution of $\rho = \rho_0(r/r_0)^{-1}$ is favored. The largest uncertainty in the mass is caused by the dust coefficient.

3.5. The Molecular Hydrogen Lines

The equatorial region in butterfly nebulae is sufficiently dense to escape ionization during most or all of the PN evolution (Balick 1987). Beintema and Pottasch (1999) report H_2 lines from 2.4 to 17 μm detected with ISO/SWS. We retrieved their pipeline-reduced data from the ISO archive. The ISO reference position is RA=17$^{\rm h}$13$^{\rm m}$44$^{\rm s}$.2, Dec=−37°06′06″.7 (*J*2000): the bright Brα core and the dark lane are covered by the ISO aperture. The observed line intensities are listed in Table 3.

The Einstein A coefficients are taken from Turner, Kirby-Docken and Dalgarno (1977). Wavelengths are calculated from the parameters in Dabrowski (1984) [1]. Fig.18 shows the (LTE) level populations of H_2, derived from these lines. The H_2 line intensities are approximately fitted with excitation temperature of $T_{\rm ex} = 700$ K and column density of $N = 6 \times 10^{19}$ cm^{-2}. The two lines at longest wavelengths (ν = 0–0, S(1) and S(2)) were observed with a larger field of view (FOV) of 14×27 arcsec^2, than the other lines (14×20 arcsec^2). Excluding these lines yields $T_{\rm ex} = 900$ K and $N = 1 \times 10^{19}$ cm^{-2}. This indicates the presence of colder gas, detected in low excitation levels only. The hot gas can be fluorescent or thermal excited. The H_2 ν=0 and ν=1 lines in NGC 6302 are fitted well with LTE. However, fluorescent excitation will cause the intensities of the

[1] www.jach.hawaii.edu/JACpublic/UKIRT/astronomy/calib/h2_s.html

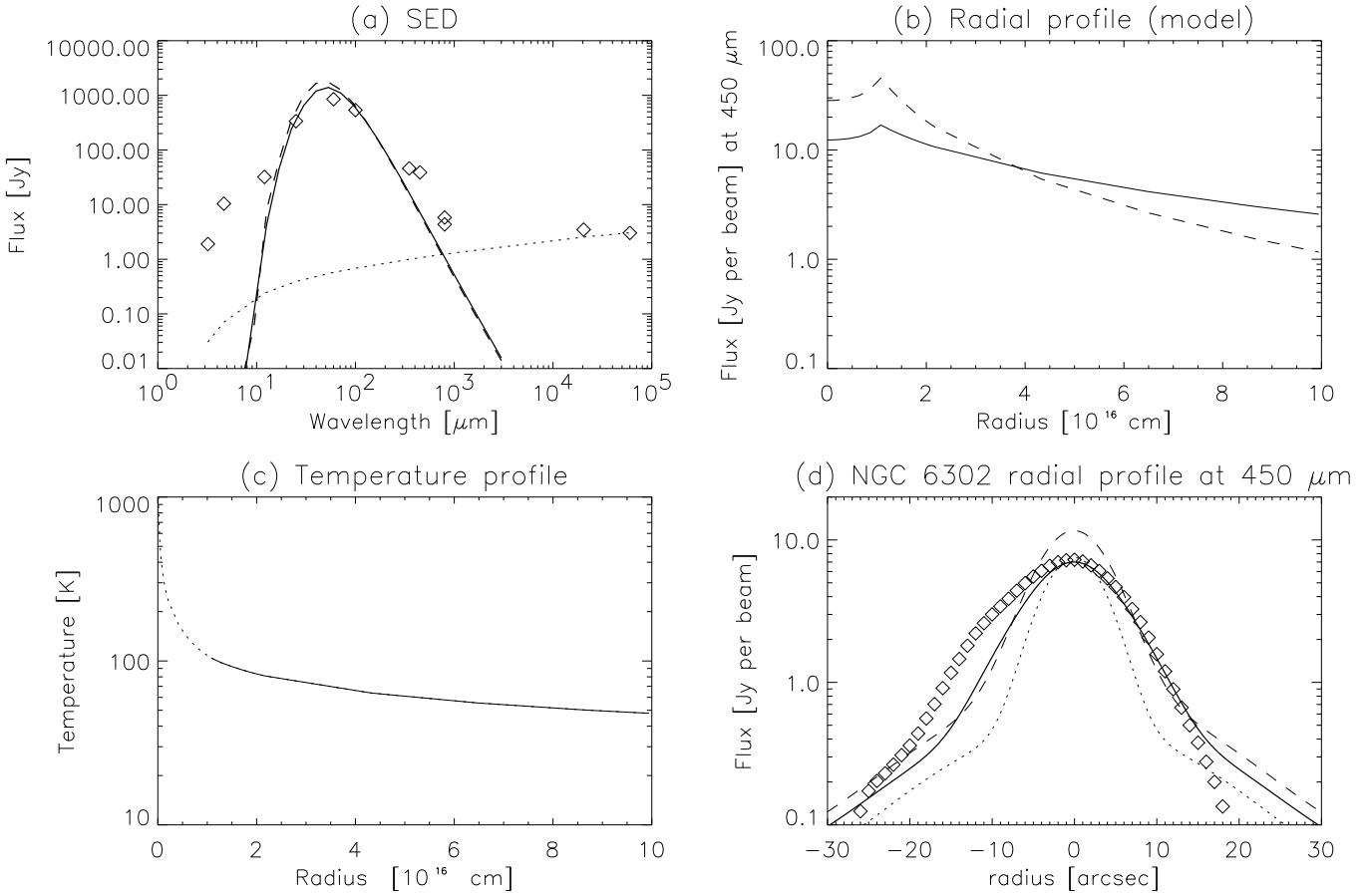

Fig. 17. (a) The SED of NGC 6302 (diamonds) and model fit with two different radial profiles. The solid line is for $\rho = \rho_0(r/r_0)^{-1}$, and the dashed line is for $\rho = \rho_0(r/r_0)^{-2}$; (b) Theoretical radial profiles; (c) Temperature profiles which do not show any difference of the density profile because the disk is optically thin in most wavelength, and radiation with the optically thick wavelength is negligible. Temperature inner than r_0 is the one for assumed gas temperature; (d) Comparison of two calculated radial profiles with the observed 450 μm profile. Observed profile is cut at brightest position along equivalent Dec line, and coordinates are different from ISAAC images. The SCUBA beam profile, whose peak is normalized to the observed peak flux, is plotted with a thin line.

v=0 and v = 1 H_2 lines resemble a 1000 K thermal, as predicted from a model for the planetary nebula NGC 7027 (Black and van Dishoeck 1987).

Davis et al. (2003) present narrow band images of the 2.121 μm H_2 v=1–0 line, and low-resolution K-band spectra in various slit positions including the infrared core and the dark lane. H_2 lines are found in all spectra, but are particularly bright in the infrared core. The cold disk (dust temperature of ~50 K; Kemper et al. (2002)) is expected to contain H I and H_2 gas. However, at low temperature the H_2 infrared lines are very weak, with the exception of the 17.035μm $v = 0 - 0$ S(1) line. For example, a column density of more than 2×10^{22} cm^{-1} is needed to emit a detectable 12.2790 μm S(2) line (more than 10^{-5} erg cm^{-2} s^{-1} sterad^{-1}) at 100 K. We suggest that H_2 molecules detected with ISO/SWS are located on the photo-heated surface of the disk, which is seen in the near-infrared. This location is consistent with Davis et al. (2003).

The total H_2 mass, using N=6 × 10^{19} cm^{-2} and the FOV of 14 × 27 arcsec^2, is $m(H_2) = 0.009\,M_\odot$. Although this includes the 17-μm line, the total H_2 mass is certainly underestimated: the cold gas will be largely undetected in the ISO/SWS observations.

3.6. The Central Star

The central star of NGC 6302 has not previously been detected (Pottasch and Beintema 1999) in direct images. Feibelman (2001) and Groves et al. (2002) claim scattered light of the central star in their spectra.

In the M_NB, NB_4.07, and NB_3.21 images (Figs. 4, 5), a compact source is present near the center of symmetry of the infrared and radio images (position (g) in Fig. 8). It has no counterpart at Hα, suggesting high extinction or non-ionized gas. The source is located at or near the center of the rectangular cavity which is seen in Fig. 4 and in the radio image (Fig. 7). This cavity could be interpreted as the hot-bubble surrounding the central star (Gómez et al. 1989). The compact source could therefore be related to the central star.

The flux of the compact source, using 0.355-arcsec aperture photometry, is 0.035, 0.022, and 0.004 Jy (9.1, 10.0, and 12.4 in magnitudes) in M_NB, NB_4.07, and NB_3.21. The ISAAC

Table 3. The observed H_2 line intensities and fitted results. The line intensity is in erg cm^{-2}s^{-1}sterad^{-1}. Model (1) is for excitation temperature of 700 K, column density of 6×10^{19} cm^{-2}, model (2) is for excitation temperature of 900 K, column density of 1×10^{19} cm^{-2}.

Transition	Wavelength [μm]	Upper level energy [cm^{-1}]	Observed $I_{H_2} \times 10^5$	FOV [arcsec^2]	$I_{H_2} \times 10^5$ Model (1)	$I_{H_2} \times 10^5$ Model (2)
0-0 S(1)	17.035	705.5	15.6	14×27	14.2	2.2
0-0 S(2)	12.279	1169.0	17.1	14×27	18.8	3.6
0-0 S(3)	9.6649	1740.4	26.4	14×20	96.4	23.9
0-0 S(4)	8.0258	2414.6	10.6	14×20	30.7	10.4
0-0 S(5)	6.9091	3187.4	28.3	14×20	56.1	27.0
1-0 O(6)	3.5007	5202.3	2.1	14×20	0.9	1.1
1-0 O(5)	3.2350	4834.7	3.6	14×20	6.7	6.9
1-0 O(3)	2.8025	4273.8	1.5	14×20	21.3	16.9
1-0 Q(5)	2.4548	5814.0	9.6	14×20	2.3	3.6
1-0 Q(3)	2.4237	4834.7	9.1	14×20	11.9	12.2
1-0 Q(1)	2.4066	4273.8	18.1	14×20	25.2	19.9

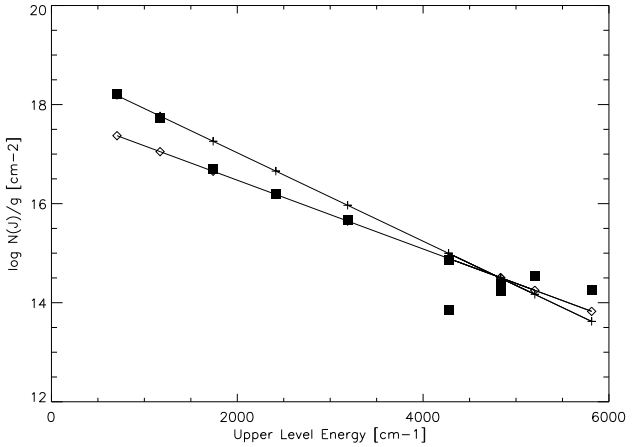

Fig. 18. Population of hydrogen molecules. Filled squares are the observed H_2 intensities by Beintema and Pottasch (1999). Two model fits are shown. One is for excitation temperature of 700 K, and column density of 6×10^{19} cm^{-2} (cross), and the other is for excitation temperature of 900 K and column density of 1×10^{19} cm^{-2} (diamond).

point spread function has a long tail; with such a small aperture of 1 FWHM, the photometric accuracy is only 0.5–1.0 mag.

The luminosity is derived from the M_NB flux, ignoring extinction. If the temperature is higher than 1×10^5 K, the resultant luminosity exceeds the Eddington Limit ($4.7 \times 10^4 L_\odot$ for a 1.4 $M_\odot$ object). The stellar temperature, estimated from Zanstra temperatures or from ionization equilibrium, is in the range 1×10^5–4.3×10^5 K (Ashley, and Hyland 1988). A temperature of 0.5×10^5 K would be needed to obtain a luminosity $L = 2.3 \times 10^4 L_\odot$, corresponding to the evolutionary track for stars with initial mass of 5.0 $M_\odot$ (Vassiliadis and Wood 1993; Blöcker 1995). Such a low temperature appears excluded if the nebula is in ionization equilibrium. Additionally, the infrared fluxes show an extremely red color. This suggests the extinction should not be ignored, and the luminosity could be even higher. Therefore, it is unlikely that the central star is directly detected.

The source could be a binary companion. A B dwarf could fit the M_NB-magnitude, as an B2–3 V star has an absolute magnitude in K-band is −1.38 (Wainscoat et al. 1992), and at the distance of 1 kpc and assuming $A(M)$ ∼2.0 mag and $K - M$=0.00, the magnitude is about 10.6 mag. However, this is an unlikely solution since the initial mass of B2 V star is 8.7 $M_\odot$ (Gray 1992), which could have evolved faster than the primary star, and should not be a dwarf now. We conclude that the infrared compact source is more likely to be circumstellar dust around the star.

4. Discussion

4.1. A warped disk

There are several symmetry axes found in NGC 6302. In the optical, the dark lane is aligned north-south, and the outer bipolar wings are seen perpendicular to the dark lane (Meaburn and Walsh 1980). In the 6 cm map, the axis is 45 degree rotated from the optical axis (Gómez et al. 1989). The Brα image confirms this inner rotation. The radio image also indicates that the inner region of the bipolar wings line up with the angled core region. Further out, the contours return to an east-west axis. The optical VLT image (Fig. 6) also shows this angling of the wings, with especially on the eastern side further emission enhancements along the angled axis, perpendicular to the inner ionized shell, up to 30 arcsec from the center. The structure gives the impression of a significant change in angle of the constraining structure close to the star, with outflows at 45 degrees from the north-south disk extending into the outer, east-west lobes. The innermost disk appears to be oriented NW-SE, along the major axis of the ionized shell which is the ionized inner edge of the disk. Further out, the disk runs NS, or even NNE-SSW. Warps in disks can occur due to torques in a multiple system, but radiative instability can also cause warping of a disk around a single star (Icke 2003).

Icke (2003) models the interaction of a hot stellar wind with a warped disk (c.f. Pringle 1996). The structures develop multipolar axes, and a bright edge along the bend disk. There are some similarities with the structures in NGC 6302, including the northern arc (the bright edge) and the angled outflows extending into the outer wings. The model develops a collimated flow where the fast wind breaks through the bend in the disk.

The HST images shows faint Hα emission NNW and SSE of the disk, at the place where the models show this developing collimated flow.

4.2. Masses of the disk and lobes

The mass of the disk and lobes are derived with three individual methods: (i) convert the gas mass from the dust extinction; (ii) combining the ionized, neutral and molecular hydrogen line observations; (iii) the disk mass derived from SED and 450 μm image fitting (sect.3.4). The nebular mass provides a lower limit on the mass of the progenitor star. The distance of NGC 6302 is taken as 1 kpc.

To derive the extinction mass of the disk, we use the ISM relation between the gas column density and $A_{\rm V}$:

$$N(H) \approx A_{\rm V}/5.3 \times 10^{-22}\,{\rm cm}^{-2}\,{\rm mag}^{-1} \quad (1)$$

(Cardelli, Clayton and Mathis 1989). The Hα extinction map (Fig. 8) shows that the disk has $A_{\rm H_\alpha} > 5$ mag, while the lobes have $A_{\rm H_\alpha} < 5$ mag. We subtract the interstellar extinction of $A_{\rm H_\alpha}$=0.91 mag. We assume $A_{\rm H_\alpha} = 1.21 A_{\rm V}$. Integrating $A_{\rm H_\alpha}$ over the region of $A_{\rm H_\alpha} > 5$ mag, and doubling the result because only the foreground disk contributes to the observed extinction, we obtain a disk mass of 0.10 $M_\odot$. The $0 < A_{\rm V} < 5$ mag region in Fig. 8 gives a mass in the lobes of 0.4 $M_\odot$. The mass in the lobes outside of Fig. 8 is not included. In total, there is least 0.5 $M_\odot$ in the central 17.8×17.8 arcsec^2 region of NGC 6302.

Gómez et al. (1989) derived ionized hydrogen mass from the 6 cm continuum flux, for a distance of 2.2 kpc. Scaling their distance to 1 kpc, the ionized hydrogen mass is $m_{\rm H\,II} = 0.02\,{\rm M}_\odot$. Rodríguez and Moran (1982) and Rodríguez et al. (1985) detect the 21 cm H I line, and derive a column density of 8×10^{20} cm, assuming a spin temperature of 100 K. The 21 cm H I was is resolved in the RA direction (Rodríguez et al. 1985) with a largest diameter of approximately 11 arcsec. We assume that H I gas is uniformly spread out over an area 3 times larger than their beam (3×14 arcsec), and we obtain $m_{\rm H\,I} = 0.02\,{\rm M}_\odot$. The H I gas may be located in, or on the edge of, the disk. The H_2 mass (Sect.3.5 is estimated as 0.009 $M_\odot$, which probably represents the excited H_2 on the surface of the disk. This H_2 mass is a lower limit.

The estimated gas masses are summarized in Table 4. The mass estimated from H_2, H I lines and 6 cm continuum emission is only 10% of the gas mass estimated from extinction. The estimate from the SED gives an even larger number, 3 $M_\odot$ in the disk.

Kemper et al. (2002) estimated a dust mass of 0.05 $M_\odot$ in the disk and 1×10^{-4} $M_\odot$ in the lobes from ISO/SWS spectra. Their dust mass is consistent with our estimate from the SED (0.03 $M_\odot$ in dust). Both estimates use the far-infrared excess, and this shows the presence of a large dust mass.

The order of magnitude difference with mass derived from the hydrogen lines suggests that most of the gas is not detected. This can only be due to cold H_2 gas, and indicates that the disk is massive, highly shielded ad molecular.

The molecular mass estimated from the CO line (Huggins et al. 1996) is 0.02 $M_\odot$ at the distance of 1.0 kpc, assuming the CO J=2–1 line is optically thin, still a factor of 30 less than the estimate from the SED. Saturation of the CO J=2–1 line may cause an underestimate of the molecular mass by a factor of ten (c.f. van der Veen and Rugers 1989). Nevertheless, NGC 6302 should have had a progenitor towards the upper limit of stellar mass which could evolve into the PN.

Table 4. Dust masses, using different methods

Gas and dust	Mass [$M_\odot$]	Location
H II	0.02	lobes
H I	0.02	disk
H_2	0.01	disk edge?
Total	0.05	
Extinction ($A_{\rm H_\alpha} > 5$)	0.1	disk
Extinction ($0 < A_{\rm H_\alpha} < 5$)	0.4	part of lobes
Total	0.5	
SED gas mass	3	disk

4.3. Disk motion and formation

The disk could have formed at the end of AGB phase, when the star has high mass-loss rate (up to 10^{-4} $M_\odot$yr^{-1}). If the disk maintained the radial velocity of the AGB phase, the current radius is about 2.1 arcsec (3.2×10^{16} cm). In this estimate, we use an expansion velocity of 20 km s^{-1} over 5×10^3 years of post-AGB and PN phase. This is only a factor of three larger than the inner radius of the shell used in SED fit (1×10^{16} cm). The disk is likely still expanding.

The disk and PN fast wind have momentum roughly $\rho_d \Delta v_d = \rho_w v_w$ where ρ_d and ρ_w are the density of the disk and outflow, and v_d and v_w are the expansion velocity of the disk and PN fast wind. v_w is taken as 1200 km s^{-1} (Meaburn and Walsh 1980). We ignore the energy loss, and assume that the collision of the PN fast wind increases the disk expansion velocity. If the density of the inner disk is $\rho_0 = 4.75 \times 10^{-18}$ g cm^{-2} (for $\rho = \rho_0 (r/r_0)^{-1}$; sect.3.4) and $\rho_w \sim 10^4$ cm^{-3}, the increase in the expansion velocity of the disk is 2×10^{-3} km s^{-1}. This means that the disk is stable against the fast wind, and can be the cause of the bipolar shape of the ionized nebula.

Post-AGB star, such as the Red Rectangle (HD 44179), can have long-lived binary disks surviving over 10^4 years (Waters et al. 1992; Jura, Balm, and Kahane 1995). However, in NGC 6302 the disk is much larger and is likely expanding: it will not survive as long as the one in Red Rectangle. The formation mechanism of the disk is not clear in NGC 6302: possibilities are binary interaction(Van Winckel et al. 1999), or the magnetic field (Matt et al. 2000).

4.4. Formation and distribution of dust grains

Both oxygen-rich dust (crystalline silicate) and carbon-rich dust (PAH) are detected in NGC 6302. Molster et al. (1999) proposed that the silicate is located in a circumstellar disk. The low temperatures of the crystalline silicate bands are 30–60 K (Kemper et al. 2002) or 65–80 K (Molster et al. 2002) suggest that this component contributes to and should be located within 450 μm image, confirming a location in the disk. This is also

confirmed from the ISO aperture (14×27 arcsec^2 in 12–28 μm) within which the crystalline silicate bands are detected. The outer part of the outflow does not contribute to the ISO spectra.

Theoretically, PAHs are formed from carbon-rich gas, and it is difficult to make PAHs in oxygen-rich environment. Where PAHs and silicates coexist in a post-AGB object, the PAHs are detected in the bipolar outflow, but not in the disk (Waters et al. 1998; Matsuura et al. 2004). For the carbon-rich star HD 44179 (Waelkens et al. 1996), this is explained with evolution from an oxygen-rich to a carbon-rich star: oxygen-rich gas is stored in the disk, while PAHs are formed in the current carbon-rich outflows. However, there is no evidence of carbon-rich gas found in NGC 6302, and this explanation fails here. Herbst (1991) suggested that carbon-rich molecules could be formed from the interstellar medium which is oxygen-rich gas by exposure to UV radiation. Photo-dissociation of CO exposed to strong UV radiation from the central star can give rise to free carbon atoms. At low densities, CO reformation may be suppressed allowing other reactions to mop up the C. Such a process has been suggested based on observations in the binary star XX Oph (Evans et al. 1999), and in novae (Evans 2001).

Shock dissociation of CO could also be considered, to avoid the problem that the intermediary products must survive long enough in the UV field to allow photo-stable large carbon rings to form. The shocks may occur in more extinct regions.

5. Conclusion

The presented images show a high mass dusty disk, optically deep even at 4μm. The Brα image shows an ionized inner shell. An infrared source near the center of the shell may be circumstellar dust close to the star. The shell is oriented at a 45-degree angle to the disk. We suggest that the disk is warped and that ionized shell is the inner edge of the disk.

Several flares and arcs are found outside of the shell. A northern arc is probably the edge of the disk. The other structures show the effect of the fast wind from the star. Both accelerating and cometary knots are found, respectively in the inner and outer outflow.

The total mass of the nebula is estimated as 3 $M_\odot$, from the fit to the SED. Extinction maps show that much of this mass is located in the massive disk. The H_2 mass is an order of magnitude lower, suggesting the disk is too cold to detect in the vibrational lines. The large extinction in the disk does not follow the usual interstellar extinction law, suggesting the presence of the large dust grains. Globally, the difference of the brightness of the east and west wings is intrinsic, and suggestive of a larger mass in the east lobe. The total mass shows that NGC 6302 has a high-mass progenitor, perhaps 5 $M_\odot$.

PAHs are found in the shell surrounding the ionized gas, and at the edge of the disk. They are located in the outflow. We propose that the PAHs have formed in oxygen-rich gas, perhaps following CO dissociation in the shock heated surface of the disk. Crystaline silicates are located in the disk.

Acknowledgements. We are grateful for the support by the ESO staff, both in preparing the observations (thanks Fernando!) and carrying out the observations. The ESO/ST-ECF Science Archive, VLA archive, ISO archive and JCMT archive were used for this research. The JCMT is operated by the Joint Astronomy Centre on behalf of the UK Particle Physics and Astronomy Research Council, the National Research Council of Canada and the Netherlands Organization for Pure Research. We thank Dr. Gómez who allowed re-publication of 6 cm data. Drs. T. Onaka and F. Kemper stimulated discussion about dust grains. M.M. thanks Dr. J.V. Buckle to rescue her from difficulties in data-reduction. This research was financially supported by PPARC grants.

References

Adams, F.C., & Shu, F.H. 1985, ApJ 296, 655
Adams, F.C., & Shu, F.H. 1986, ApJ 308, 836
Allamandola, L.J., Tielens, G.G.M., Barker, J.R. 1989, ApJS 71, 733
Anderson, J., King, I.R., 2003, PASP 115, 113
Ashley, M. C. B., & Hyland, A. R. 1988, ApJ 331, 532
Balick, B. 1987, AJ, 94, 671
Balick, B., Frank, A., 2002, ARA&A 40, 439
Beintema, D.A., & Pottasch, S.R. 1999, A&A 347, 942
Black, J.H., & van Dishoeck, E.F. 1987, ApJ 322, 412
Blöcker, T. 1995, A&A 299, 755
Bohigas, J. 1994, A&A 288, 617
Cardelli, J.A., Clayton, G.C., & Mathis, J.S. 1989, ApJ 345, 245
Casassus, S., Roche, P.F., & Barlow, M.J. 2000, MNRAS 314, 657
Cox, P., Maillard, J.P., Huggins, P.J., et al. 1997, A&A 321, 907
Dabrowski, I. 1984, Can, J. Phys 62, 1638
Davis C.J., Smith, M.D., Stern, L., Kerr, Th.H., Chiar, J.E. 2003, MNRAS 344, 262
Dudziak, G., Walsh, J.R., 1997, The 1997 HST Calibration Workshop with a new generation of instruments, eds. S. Casertano et al., Space Telescope Science Institute, p. 338.
ESO Press Release 06, 1998
Evans, A. 2001, Ap&SS 275, 131
Evans, A., Eyres, S. P. S., Hauschildt, P.H., Allard, F. 1999, The Universe as Seen by ISO, eds. P. Cox & M.F. Kessler, ESA-SP 427, 305
Feibelman, W.A. 2001, ApJ 550, 785
Gómez, Y., Rodríguez, L.F., Moran, J.M., Garay, G. 1989, ApJ 345, 862
Gray, D.F., The observation and analysis of stellar photospheres', Second edition, 1992, Cambridge University Press
Groves, B., Dopita, M.A., Williams, R.E., Hua, C.T. 2002, PASA 19, 425
Herbst, E. 1991, ApJ 366, 133
Hogerheijde, M.R., Sandell, G., 2000, ApJ 534, 880
Hoare, M.G., Roche, P.F., & Clegg, R.E.S. 1992, MNRAS 258, 257
Holland, W.S., Robson, E.I., Gear, W.K., et al. 1999, MNRAS 303, 659
Hua, C.T., M.A. Dopita, M.A., & Martinis, J. 1998, A&AS 133, 362
Huggins, P.J., Bachiller, R., Cox, P., Forveille, T. 1996, A&A 315, 284
Hummer, D.G., & Storey, P.J. 1987, MNRAS 224, 801

Hummer, D.G., & Storey, P.J. 1995 MNRAS 272, 41
Icke V. 2003, A&A 405. L11
Itoh, N., Sakamoto, T., Kusano, S., Nozawa, S., Kohyama, Y. 2000, ApJS 128, 125
Jura, M., Balm, S.P., Kahane, C., 1995, ApJ 453, 721
Karzas, W.J., Latter, R., 1961, ApJS 6, 167
Kastner, J.H., Weintraub, D.A., Gatley, I., Merrill, K.M., Probst, R.G. 1996, ApJ 462, 777
Kemper, F, Molster, F.J., Jäger, C., Waters, L.B.F.M. 2002, A&A, 394, 679
Kwok, S. 1982, ApJ, 258, 280
Kwok, S. 2000, 'The Origin and Evolution of Planetary Nebulae', Cambridge University Press
Latter, W.B., Kelly, D.M., Hora, J.L., Deutsch, L.K. 1995 ApJS 100, 159
Latter, W.B., Dayal, A., Bieging, J.H., Meakin, C., Hora, J.L., Kelly, D.M., Tielens, A.G.G.M. 2000, ApJ 539, 783
Léger, A., & Puget, J.L. 1984, A&A 137, L5
Lester, D.F., & Dinerstein, H. L. 1984, ApJ 281, L67
Liu, X.-W., Barlow, M.J., Danziger, I.J., Clegg, R.E.S. 1995, MNRAS 273, 47
Lopez, B., Tessier, E., Cruzalebes, P., Lefèvre, J., Le Bertre, T. 1997, A&A 322, 868
López-Martín, L., Raga, A.C., Mellema, G., Henney, W.J., Cantó, J., 2001, ApJ 548, L288
Lord, SD 1992, NASA Technical Memor. 103957
Mathis, J.S. 1999, Allen's Astrophysical Quantities, fourth edition, Springer
Matsuura, M., Zijlstra, A.A., Molster, F.J., et al. ApJ, in press
Matt, S., Balick, B., Winglee, R., Goodson, A., 2000, ApJ 545, 965
Meaburn, J., & Walsh, J.R. 1980, MNRAS 193, 631
Mennickent, R.E., & Vogt, N. 1988, A&AS 74, 497
Milne, D.K., & Aller, L.H. 1975, A&A 38, 183
Milne, D.K., & Aller, L.H. 1982, A&AS 50, 209
Molster, F.J., Lim, T.L., Sylvester, R.J., et al. 2001, A&A 372, 165
Molster, F.J., Waters, L.B.F.M., & Tielens, A.G.G.M. 2002, A&A 382, 222
Molster, F.J., Yamamura, I., Waters, L.B.F.M. et al. 1999 Nature 401, 563
Moorwood, A., Cuby, J.G., Ballester, P. et al. 1999, ESO Messenger 95, 1
Nomura, H. 2002, ApJ 567, 587
Nomura H., & Millar, T.J. 2004, A&A in press (astro-ph/0311246)
O'Dell, C.R., Balick, B., Hajian, A.R., Henney, W.J., & Burkert, A., 2002, AJ 123, 3329
Omont, A. 1986, A&A 164, 159
Payne H. E., Phillips J. A., & Terzian Y. 1988, ApJ 326, 368
Peimbert, M. 1978, IAU Symposium 76, Planetary Nebulae, ed. Y. Terzian (Dordrecht), p215
Persi, P., Cesarsky, D., Marenzi, A.R., Preite-Martinez, A., Rouan, D., Siebenmorgen, R., Lacombe, F., Tiphene, D. 1999, A&A 351, 201
Phillips, J.P., Reay, N.K., & White, G.J. 1983 MNRAS, 203, 977
Pottasch, S. R., Beintema, D., Dominguez-Rodriguez, F.J., Schaeidt, S., Valentijn, E., Vandenbussche, B. 1996, A&A 315, L261
Pottasch, S. R. & Beintema, D. A. 1999, A&A, 347, 975
Pringle, J.E. 1996, MNRAS 281, 357
Roche, P. F., & Aitken, D. K. 1986, MNRAS 221, 63
Roche, P.F. Lucas, P.W., Hoare, M.G., Aitken, D.K., Smith, C.H. 1996, MNRAS 280, 924
Rodríguez, L.F., & Moran, J.M. 1982, Nature 299, 323
Rodríguez, L.F., Garcia-Baretto, J.A., Canto, J., Moreno, M.A., Torres-Peimbert, S., Costero, R., Serrano, A., Moran, J.M., Garay, G. 1985, MNRAS, 215, 353
Rowlands, N., Houck, J.R., Herter, T. 1994, ApJ, 427, 867
Sahai R., Bujarrabal V., Castro-Carrizo A., & Zijlstra A.A. 2000, A&A 360, L9
Sahai R., Trauger, J.T. 1998, AJ 116, 1357
Sellgren, K., Tokunaga, A. T., Nakada, Y. 1990, ApJ 349, 120
Tokunaga, A.T., 1999, Allen's Astrophysical Quantities, fourth edition, Springer
Turner, J., Kirby-Docken, K., & Dalgarno, A. 1977, ApJS 35, 281
Ueta, T., Meixner, M., Bobrowsky, M., 2000, ApJ 528, 861
van der Bliek, N.S., Manfroid, J., & Bouchet, P. 1996, A&AS 119, 547
van der Veen, W.E.C.J., Rugers, M., 1989, A&A 226, 183
Van Winckel, H., Waelkens, C., Waters, L.B.F.M. 1995, A&A 293, L25
Van Winckel, H., Waelkens, C., Fernie, J. D., Waters, L.B.F.M. 1999, A&A 343, 202
Vassiliadis, E., & Wood, P.R. 1994, ApJS 92, 125
Wainscoat, R.J., Cohen, M., Volk, K., Walker, H.J., Schwartz, D.E., 1992, ApJS 83, 111
Waters, L.B.F.M., Trams, N.R., Waelkens, C. 1992, A&A 262, L37
Waters, L.B.F.M., Molster, F.J., de Jong, T. 1996, A&A 315, L361
Waters, L.B.F.M., Cami, J., de Jong, T., et al. 1998, Nature 391, 868
Wolf, S., Hillenbrand, L.A. 2003, ApJ 596, 603
Waelkens, C., Van Winckel, H., Waters, L.B.F.M., Bakker, E. J. 1996, A&A 314, L17
Williams, S., PhD thesis, UMIST 2003
Woodward, C.E., Pipher, J.L., Shure, M., Forrest, W.J., Sellgren, K. 1989, ApJ 342, 860
Zijlstra, A.A. 2001a, Ap&SS 275, 79
Zijlstra, A.A., Chapman, J.M., te Lintel Hekkert, P., et al., 2001, MNRAS 322, 280